AGU PUBLICATIONS

JGR

Journal of Geophysical Research: Space Physics

RESEARCH ARTICLE
10.1002/2017JA024666

Key Points:
- Deuterium Lyman alpha brightness in the upper atmosphere of Mars is highly variable, peaking just after southern summer solstice
- Martian limb D brightness varies on timescales that are similar to those of water vapor variations lower in the atmosphere
- Deuterium variability may be due to seasonal factors such as regional dust storm activity and subsequent lower atmospheric circulation

Correspondence to:
M. Mayyasi,
majdm@bu.edu

Citation:
Mayyasi, M., Clarke, J., Bhattacharyya, D., Deighan, J., Jain, S., Chaffin, M., … Jakosky, B. (2017). The variability of atmospheric deuterium brightness at Mars: Evidence for seasonal dependence. *Journal of Geophysical Research: Space Physics*, *122*. https://doi.org/10.1002/2017JA024666

Received 10 AUG 2017
Accepted 9 OCT 2017
Accepted article online 16 OCT 2017

The Variability of Atmospheric Deuterium Brightness at Mars: Evidence for Seasonal Dependence

Majd Mayyasi[1], John Clarke[1], Dolon Bhattacharyya[1], Justin Deighan[2], Sonal Jain[2], Michael Chaffin[2], Edward Thiemann[2], Nick Schneider[2], and Bruce Jakosky[2]

[1]Center for Space Physics, Boston University, Boston, MA, USA, [2]LASP, University of Colorado Boulder, Boulder, CO, USA

Abstract The enhanced ratio of deuterium to hydrogen on Mars has been widely interpreted as indicating the loss of a large column of water into space, and the hydrogen content of the upper atmosphere is now known to be highly variable. The variation in the properties of both deuterium and hydrogen in the upper atmosphere of Mars is indicative of the dynamical processes that produce these species and propagate them to altitudes where they can escape the planet. Understanding the seasonal variability of D is key to understanding the variability of the escape rate of water from Mars. Data from a 15 month observing campaign, made by the Mars Atmosphere and Volatile Evolution Imaging Ultraviolet Spectrograph high-resolution echelle channel, are used to determine the brightness of deuterium as observed at the limb of Mars. The D emission is highly variable, with a peak in brightness just after southern summer solstice. The trends of D brightness are examined against extrinsic as well as intrinsic sources. It is found that the fluctuations in deuterium brightness in the upper atmosphere of Mars (up to 400 km), corrected for periodic solar variations, vary on timescales that are similar to those of water vapor fluctuations lower in the atmosphere (20–80 km). The observed variability in deuterium may be attributed to seasonal factors such as regional dust storm activity and subsequent circulation lower in the atmosphere.

1. Introduction

The content of primordial water at Mars is presently under investigation in order to determine whether the planet was once "wet and warm" or "cold and icy" (Head & Marchant, 2014). Toward the goal of determining ancient water reservoirs, the water content and its variability with time, at the present epoch, are being measured and characterized. Unraveling the properties of water and its isotopologues, as they vary throughout the Martian water cycle with altitude and season, will allow for more accurate extrapolation of these species back in time.

At the present time, water at Mars is available in the form of subsurface ice, surface ice, ice in atmospheric clouds, and atmospheric vapor. These various forms of water interact in a hydrological cycle that includes, in increasing distance from the surface, sublimation of polar ice, atmospheric mixing and circulation, condensation, photodissociation by sunlight, chemical reactions, transport to higher altitudes, and ultimately, loss into outer space (e.g., Aleshin, 2004; Bertaux & Montmessin, 2001; Haberle & Jakosky, 1990; Jakosky, 1983; Jakosky & Farmer, 1982; McElroy & Donahue, 1972).

The relative abundance of two water-based components, hydrogen (H), and deuterium (D), has been widely used to quantify the water retention rate, from the surface of a planet through its upper atmosphere, by analyzing the preferential escape of the lighter species with respect to its heavier isotope (e.g., Bruner & Wilson, 1969; Donahue, 1969; Jakosky, 1991). H and D resonantly scatter solar Lyman α at 121.567 and 121.534 nm, respectively; therefore, the emission spectra from these two UV lines can be used to determine the brightness of H and D. Subsequent simulations can then be applied to determine the abundances of these species based on their observed UV emission properties (de Bergh, 1992).

Mars hydrogen and water spectral lines are bright and have been observed using ground-based, space-based, and remote sensing instruments for decades (Bertaux & Montmessin, 2001; Clarke et al., 2006, 2014, 2017; Krasnopolsky, 2015; Mahaffy et al., 2015; Novak et al., 2011; Owen et al., 1988; Villanueva et al., 2012; Webster et al., 2013). Recent discoveries have found there to be a seasonal dependence to the H abundance in the Martian exosphere and lower atmosphere (Aoki et al., 2015; Chaffin et al., 2014, 2017; Clarke et al., 2014,

2017; Fedorova et al., 2017; Halekas, 2017; Maltagliati et al., 2011, 2013; Montmessin et al., 2005; Villanueva et al., 2015). Until recently, there were limited observations of D Lyman α emissions from the upper atmosphere of Mars (Bertaux et al., 1992; Clarke et al., 2006; Krasnopolsky et al., 1998). The data obtained by the high-resolution echelle mode of the Imaging Ultraviolet Spectrograph (IUVS) instrument on board the NASA Mars Atmosphere and Volatile Evolution (MAVEN) mission (Jakosky, 2015, McClintock et al., 2015) allows the separate emissions of H and D Lyman α to be resolved and the properties of deuterium at Mars to be more comprehensively examined.

We present the longest baseline of continuous observations of upper atmospheric deuterium—made at any planet—in order to characterize its brightness and variability. The timeline of observations extends 15 Martian months and is conducive to investigating numerous drivers of variability and their respective timescales. This analysis provides constraints on the temporal changes in the observed deuterium brightness and will improve calculations of the present-day and extrapolated historic abundances of D to H atoms in the upper atmosphere of Mars.

The next section provides a description of the observations used in this work. The observed variability in D brightness is shown in section 3. Various sources of variability are considered and discussed in section 4. Summary and findings are provided in section 5. Details of the observations that are useful for reproducing the results of this work are provided in the Appendix A.

2. Observations

The MAVEN IUVS remote sensing instrument makes measurements throughout most of the MAVEN orbit. To optimize detection of atmospheric emission features, the instrument line of sight is generally directed at a sunlit region of the planet. These observations include measurements made of the disk, limb, and corona of Mars. The observations used for the present analysis are limited to IUVS echelle observations where the line of sight along the aperture was pointed at the sunlit limb of Mars. The limb-pointed subset of the available data is the longest available to consistently cover regions where deuterium is likely to be detected. These data include observations where the minimum ray height (MRH) altitude above the tangent point of the line of sight (LOS) vector from the spacecraft varied between 0 and 400 km above the surface of the planet.

Operational requirements dictated the use of different binning schemes of the full 1,024 × 1,024 pixel detector throughout the mission where each binning scheme captured a different subset of the detector. All the IUVS echelle binning schemes used to date included the portion on the detector that measures the H and D Lyman α emissions. Additional constraints resulted in observations being made, while the spacecraft was in different segments of its orbit around Mars. Subsequently, a different number of limb scans was obtained for each orbit. Additional details of the observational modes are described in Appendix A.

3. Results

The echelle observations described in Table A1 were systematically reduced and calibrated as described in Mayyasi et al. (2017). Examples of D and H spectra are given in Clarke et al. (2017). The deuterium Lyman α is a faint emission compared with hydrogen Lyman α. Therefore, spectra were coadded in order to improve the signal-to-noise ratio and obtain a more robust emission spectrum for D. Below 0 km MRH altitude, the LOS of the instrument was pointed at the disk, and above 400 km MRH altitude, the D Lyman α optically thin emission is too faint to regularly detect. Therefore, data from each epoch where the LOS was pointed at the sunlit limb were averaged for all observations between 0 and 400 km for each limb scan. The brightness of D Lyman α, in kilorayleigh (kR), is shown in Figure 1 as a function of orbit number, time, and subsolar longitude, L_s.

Uncertainties in the data are dominated by the detector noise and are determined from the measured noise in a Lyman α emission-free region of the IUVS FUV detector used in echelle mode (Mayyasi et al., 2017). Brightness values that were within the 3 sigma detection limits are considered upper limits and are indicated by having the lower error bar drawn as a downward pointing arrow. Uncertainties were larger early in the mission due to the shorter integration times used to obtain those limb observations (1.4 and 3.4 s, from Table A1, were changed to 29.4 s later in the mission). The LOS of the frames used to determine the D brightness spans a range of solar zenith angles (SZA) across the 0.06° × 1.7° aperture used for echelle observations.

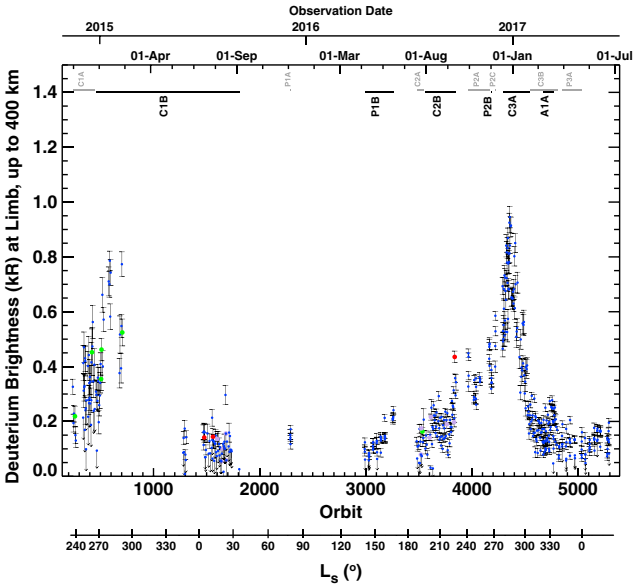

Figure 1. The orbit-averaged integrated emission brightness (in kilorayleigh) of deuterium Lyman α at Mars observed by the IUVS echelle channel for a dayside and limb-pointed LOS. Observations span approximately 1.3 Mars years and are averaged by scans in each orbit, where the line of sight MRH altitude did not exceed 400 km. Uncertainties in the measurements are shown as vertical error bars. Brightness values within 3 sigma of the noise level are considered upper limits, and their uncertainties are denoted by downward pointing arrows. Red, green, and purple data points denote when solar energetic particles, solar flares, and auroral events, respectively, were recorded at Mars. These events are described further in section 3.1. The subsolar longitude (L_S), in degrees, is shown below the orbit axis for reference. The dates of these observations are shown on the top horizontal axis. The epochs of the observations are labeled above the data and described in Table A1. Dates of transient event orbits are listed in Table A2.

This SZA range depends on the angle of the aperture with respect to the planet surface at the tangent point of the observations as well as on the distance between the spacecraft and the tangent point. The average SZA across the aperture, spanned by all frames used for a limb scan, was used to separate dayside (average SZA $\leq 90°$) from nightside data (average SZA $> 90°$).

Each data point shown in Figure 1 represents the average deuterium brightness derived from multiple coadded Lyman α spectra. The variation in limb geometry contributes to the scatter of points from orbit to orbit; however, the overall changes in D emission are much larger than this. The averaging done here therefore consistently accounts for the effects of any limb brightening that appears along the line of sight.

There were several weeks when no echelle dayside data were available, for example, when the orbital periapse was on the nightside of Mars. However, despite the gaps in data coverage, there are notable peaks in D Lyman α brightness near the two perihelion passes (L_s ~250°) observed with MAVEN to date. The overall variations in D brightness are much larger than the changes in solar Lyman α flux at Mars. Deuterium Lyman α emission brightness can vary due to a combination of varying density and/or temperature of atmospheric deuterium atoms. In order to derive the density profile for D that best matches the observations, we assume a temperature that is determined from an energy balance with the remaining neutral atmosphere, predominantly CO_2. The derived D density also factors in chemical reactions and flux of atoms from the lower atmosphere balanced against its escape into space. The present work analyzes the variability of D brightness, while efforts are underway to model and interpret the subsequent D density and its variability.

The source(s) of the fluctuations observed in Martian D Lyman α are examined against both external and internal drivers. External drivers include solar events such as coronal mass ejections (CMEs) and solar flares. Such solar events may produce solar energetic particles (SEP) that directly deposit their energies into the atmosphere and produce localized heating and potentially enhanced deuterium emission. Internal drivers include dust storms due to seasonal effects, topography, and atmospheric circulation patterns. Dust storms result in atmospheric heating that is more globally widespread across the planet and occurs over longer timescales than typical solar events and can also lead to upwelling of water from the lower atmosphere into the middle atmosphere (e.g., Tamppari et al., 2003; Withers & Pratt, 2013). These effects would also potentially increase the H and D content of the upper atmosphere (Fedorova et al., 2017). External events may increase the D brightness due to enhancing its neutral temperature. Other ambient atmospheric processes such as gravity waves may also contribute to heating thermospheric deuterium. Internal events may enhance D brightness due to increased abundance from moving water upward from lower altitudes. External drivers, such as solar flares, could potentially catalyze the chemical production of D to increase its abundance. Careful modeling is required to separate and quantify these effects and will be the subject of future work.

Remarkably, MAVEN arrived at Mars at the same time that a CME, a solar flare, the near approach of a comet (C/2013 A1 Siding Spring), and a regional dust storm were all impacting the planet's atmosphere. Subsequently, an influx of solar energetic particles (SEP) from the solar wind, CME, and flares collectively tipped the energy balance of the upper atmosphere of the planet. Decoupling the effects from these simultaneous triggers on limb D brightness with the limited early mission echelle data set is not likely. However, the repeatability and timescales with which these events are expected to impact the Martian atmosphere can be useful for gaining further insights, as discussed below.

3.1. Variability Due To Transient Events

Solar energetic particles may be carried into the atmosphere of Mars by the solar wind, solar flares, and/or in conjunction with coronal mass ejections. Detections of these sporadic events have been catalogued by the solar energetic particles (SEP) instrument onboard MAVEN (Larson et al., 2015; Lee et al., 2017). Solar wind-triggered SEP events affected echelle dayside orbits 1560 and 3838. Echelle observations in orbit 3838 (shown in red in Figure 1) show a higher D brightness of 0.44 kR. This is nearly a factor of 2 enhancement from the 20 orbit average of D brightness of 0.29 kR, centered about the event. The D observed from orbit 1560 was not significantly brighter than adjacent orbits and was calculated to be 0.14 kR. This is enhanced by only 27% above the 0.11 kR brightness determined from a 20 orbit average centered about the event. A CME that triggered SEP events affected echelle dayside orbit 1476. D observed in this orbit, also highlighted in red, is not significantly brighter than in adjacent orbits.

Auroral events were also recorded during the echelle observations presented here. These affected orbits 1600, 1640, 1648, 1682, 1686, 3520, 3524, 3602, 3614, 3764, and 3832. These orbits are shown in purple in Figure 1. The auroral events may be attributed to several triggers (Bertaux et al., 2005; Schneider et al., 2017) that may affect more than one orbit. However, all D measurements for aurora coincident and adjacent orbits were not significantly brighter than non-aurora counterparts.

Several M-class flares overlapped with echelle dayside observations of the limb. These include orbits 260, 420, 506, 510, 706, and 3534. The flare-affected orbits are shown in green in Figure 1. The M-class flare recorded for echelle orbit 420 was a category 8.7, the largest of all the recorded flares that overlapped with echelle dayside limb observations. Deuterium observed in echelle orbit 420 was brighter than in adjacent orbits. The remaining M-class flares that occurred during the times when echelle limb data were being taken ranged in strength between categories 1.6 and 7.6. The observed D brightness in these orbits was not significantly enhanced with respect to adjacent nonflare affected orbits.

X-rays are typically absorbed by the neutral atmosphere between 80 and 100 km altitude at Mars to produce ionized plasma (Haider et al. 2011). The enhanced X-ray flux from flares perturbs the neutral atmosphere and may possibly increase photochemical production of deuterium due to enhanced photodissociation of water and its isotopes at the altitudes where these photons are absorbed (Thiemann et al., 2015; Yung et al., 1988), leading to an increased flux of H and D to the upper atmosphere. In the time span of the observations used here, no X-class flares were observed at Mars during times that overlapped with IUVS echelle limb measurements.

No echelle measurements of the Martian limb were made near the passage of comet Siding Spring. The comet closest approach to Mars occurred on 20 October 2014. The first of the echelle limb observations (orbit 240) were taken on 12 November 2014, about 3 weeks after closest approach. The perturbations on the neutral atmosphere and ionosphere of Mars produced by the comet after closest approach were found to dissipate within a few days of closest encounter (Benna et al., 2015). There were also no significant changes to the H Lyman α emission during the passage of the comet from Hubble Space Telescope (HST) observations (Bhattacharyya et al., 2015, 2017). Therefore, none of the variations observed in deuterium brightness from the Martian dayside limb are likely to be due to the passage of Siding Spring.

The time to complete a single limb scan varied from ~ 1 to 30 min. The time between consecutive dayside limb scans in the echelle data set varied from a few minutes to several months. All of the transient events described here, however, occurred during orbits where there were echelle dayside measurements available either prior or subsequent to the event (or both), to within a week of the event. The effects of these transient events on D brightness measurements appear to be localized to single limb scans. Therefore, in the few cases where the D brightness was enhanced due to a transient event, the timescale can be constrained to vary between minutes to an upper limit of a week.

3.2. Variability Due To Solar Rotation

The Sun's ~28 day rotation period exposes Mars to varying solar UV flux depending on active regions and their distribution (e.g., Fröhlich & Lean, 2004). Since D is produced from photodissociation of water isotopologues and subsequent chemical reactions, a small-scale (day-to-day) variability in D brightness may be attributed to the solar rotation cycle (Clarke et al., 2017). To remove the effects of this variability, averages of the observations were made for each continuous block of 28 days. The solar rotation adjusted data are

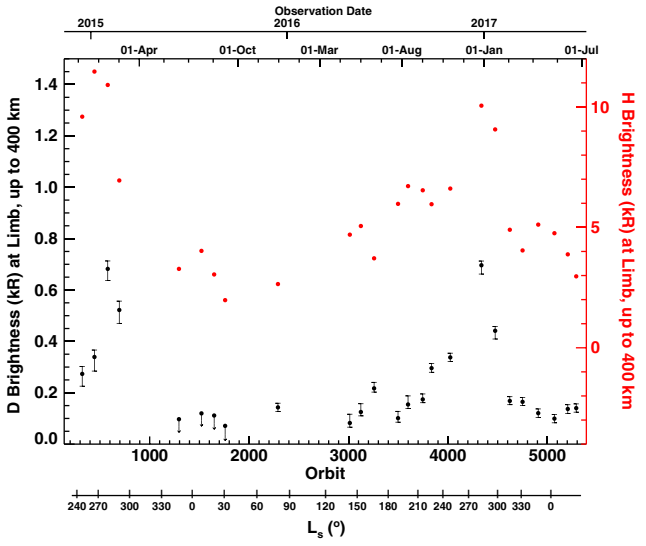

Figure 2. The solar rotation averaged limb brightness of D (black circles) and H (red circles) Lyman α emissions. Vertical bars represent the averages of the uncertainties used to determine each data point. The H Lyman α emission brightness, derived from the same data as D, is shown for reference. Deuterium brightness values within 3 sigma of the noise level are considered upper limits, and their uncertainties are denoted by downward pointing arrows. Uncertainties in the H brightness are negligible. D brightness values follow the *y* axis scale on the left. H brightness values follow the *y* axis scale on the right. IPH contributions to the H limb data are nonnegligible and have not been removed from the brightness values shown here.

shown in Figure 2 for both D and H Lyman α emissions. This averaging also minimizes the variability in D brightness introduced by transient event enhancements described in the previous section.

In Figure 2, vertical error bars represent the averaged uncertainties from the individual orbits that occurred over the 28 day period. H Lyman α brightness is measured by the IUVS echelle channel using a similar region on the FUV detector as D. The H brightness has been scaled for visibility and shown for reference. The trends in D and H variability are similar but not directly comparable since the latter includes an interplanetary hydrogen (IPH) Lyman α component that has not been removed. The brightness of IPH can vary between ~0.2 kR and ~1.4 kR, depending on the direction of the instrument line of sight, the location of Mars in its orbit, and the relative speed of the spacecraft with respect to the interplanetary flow (Ajello et al., 1994; Clarke et al., 1998; Quémerais et al., 2008). We therefore defer the non-trivial derivation of the IPH-corrected H brightness at the limb of Mars to future work.

The resulting solar rotation-averaged brightness of D Lyman α more clearly shows longer-scale variability (order of months) in the data. A peak brightness of 0.68 ± 0.05 kR occurred around L_s of 280°, near orbit 580. Another peak in D brightness of 0.70 ± 0.03 kR occurred around L_s 285°, near orbit 4340.

The echelle observations shown here were made during the declining activity phase of Solar Cycle 24, when the Sun was less active at its maximum than in previous cycles. The solar Lyman α flux at Mars, measured by the MAVEN Extreme Ultraviolet Monitor (EUVM) instrument Lyman α channel (Eparvier et al., 2015), decreased by ~25%, during the mission observations shown here, when compared with consecutive times in Mars's orbit at similar L_s (Thiemann et al., 2017).

3.3. Seasonal Variability

The production of D and H Lyman α in the atmosphere of Mars is dependent on the flux of solar EUV radiation, which acts to dissociate water, drive ion and neutral reactions, etc. Therefore, the brightness of Martian UV emissions is expected to increase close to perihelion compared with when the planet is farther from the Sun in its orbit. Observations of H Lyman α emissions from the Martian corona have shown large seasonal variations (Bhattacharyya et al., 2015; Chaffin et al., 2014; Chaufray et al., 2015; Clarke et al., 2014, 2017). With the availability of D limb observations at Mars for the first time at the timescales provided by MAVEN, the variability of D brightness can be evaluated as well for a comparison of the isotopic variability.

The dayside limb observations used here span 15 Mars months. Data gaps notwithstanding observations at similar seasons (L_s values) exist from separate Mars years. To evaluate the brightness trends consistently, a correction was made to account for variations in solar Lyman α flux between the observations made in the first Mars year (MY32) to the second (MY33). This correction was done by scaling the observations from MY32, (L_s 240°–360°; for orbits 240–1400) down by 25%, in accordance with measured EUVM solar Lyman α flux variations. This scaling normalizes the solar flux to the values measured during MY33 where more complete annual deuterium data coverage exists and allows for the remaining variations in solar Lyman α flux due to orbital distance to be more evenly evaluated as a function of season (L_s).

The resulting annual trends of limb deuterium brightness are shown in Figure 3 for MY32 (green circles) and MY33 (blue circles). The peak deuterium brightness occurred at L_s = 290° ± 17° (the uncertainty in L_s at the peak is due to the 28 day averaging described previously). For reference, Mars perihelion occurs at L_s 251° and the southern summer season spans L_s 270° (southern summer solstice) to L_s 360°.

Previous Hubble Space Telescope (HST) observations of the Martian hydrogen corona showed that the Lyman α brightness increased as the planet approached perihelion and decreased as Mars moved farther

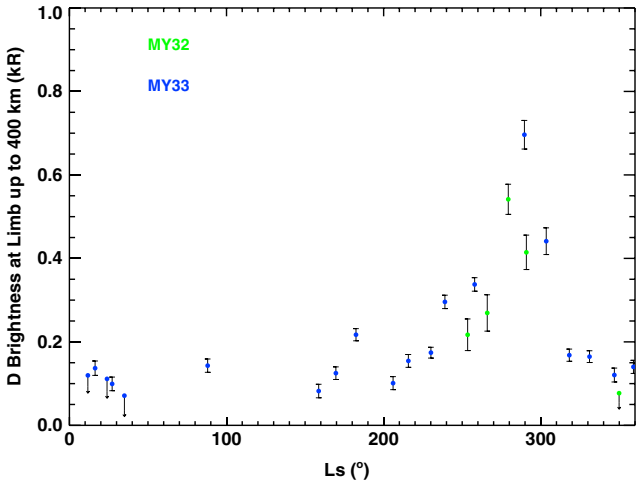

Figure 3. The solar rotation averaged limb brightness of D as a function of subsolar longitude (L_s), with overlapping data from 2 Mars years. Data from the first partial Mars year (MY32) are shown as green circles. The observations from the second year (MY33) are shown as blue circles. The data from MY32 have been scaled down by 25% to reduce variations in brightness introduced by the declining solar Lyman α flux measured by MAVEN EUVM. Vertical bars represent the averages of the uncertainties used to determine each data point. Brightness values within 3 sigma of the noise level are considered upper limits, and their uncertainties are denoted by downward pointing arrows.

away (Bhattacharyya et al., 2015). A peak brightness was estimated to occur between perihelion and southern summer, at L_s ~260°. This is consistent with measurements made of exospheric hydrogen using the MAVEN Solar Wind Ion Analyzer (SWIA) instrument (Halekas et al., 2015). Using the SWIA measurements of solar wind protons charge exchanging with the neutral H coronal atoms as well as recent HST observations as Mars crossed perihelion and southern summer solstice, inferred peak column densities of H in the corona were found to vary seasonally with a peak occurring closer to southern summer solstice than perihelion (Halekas, 2017). The H limb brightness observed with echelle channel in the data used here would need to remove IPH contributions before making comparisons to H brightness variations observed in the corona.

The peak observed in echelle measured D brightness occurred after the onset of southern summer and is offset by a few degrees in L_s from the observed coronal H peak brightness derived by HST and SWIA observations. To first order, the enhanced brightness leading up to the peak may have been similarly triggered by seasonal changes as found for H and that are related to the location of Mars in its orbit and the time-averaged insolation. However, there may be additional drivers that enhance production of D at the limb and that last beyond perihelion and southern summer onset that are offset by several days to a few weeks after the H coronal brightness is observed to peak. These variations may be associated with processes closer to the surface of Mars that are related to atmospheric dynamics lower in the atmosphere (e.g., Fedorova et al., 2017; Maltagliati et al., 2011; Trokhimovskiy et al., 2015).

3.4. Variability Due To Latitude and Dust Storm Effects

D Lyman α is a faint emission (typically ~0.5% of the brightness of H), and it drops off much more steeply with altitude above the limb than the H brightness. As an optically thin emission, the brightness variability of D Lyman α is representative of its abundance along the line of sight. At the proximity of deuterium to the surface along the line of sight compared with the H extended corona observations, properties intrinsic to the planet such as dust storms produced by orbital, topographical, and hemispherical effects can potentially influence the abundance and therefore the observed brightness of deuterium by supplying added water and hydrogen into the upper atmosphere.

Regional dust storms at Mars typically originate in one hemisphere and may migrate to another (e.g., Fernández, 1998). In Figure 4, the D brightness observed by MAVEN IUVS is shown for three latitudinal bands: northern hemisphere (for observations made where the LOS tangent point latitude ranged between 30° and 90°N), southern hemisphere (for observations made where the LOS tangent point latitude ranged between 30° and 90°S), and equatorial region (for observations made where the LOS tangent point latitude ranged between 30°N and 30°S). In each of these three regions, the MAVEN echelle spectra have been averaged for each orbit scan by filtering the LOS latitude. Resulting brightness values have been averaged to remove transient events, solar rotation effects, and have been adjusted for solar activity variability, as discussed previously for the whole data set. The times of Mars perihelion (L_s ~250°) and southern summer solstice (L_s 270°) are shown in gray vertical dashed lines for reference.

Regional dust storms have an annual periodicity. The regional dust storms observed at Mars are categorized in chronological order as Type A, Type B, and Type C storms. A study that collected 5 Mars years of observations made with the Mars Climate Sounder instrument on Mars Reconnaissance Orbiter (MRO) and the Thermal Emission Spectrometer instrument on Mars Global Surveyor (MGS) determined statistical properties of the three regional dust storms (Kass et al., 2014). Type A dust storms initiate along the northern baroclinic zone then flow down the equator to lower latitudes to trigger significant dust lifting in the southern hemisphere and heating in both hemispheres. Type B storms, confined to the southern hemisphere, are initiated by a combination of seasonal effects of winds generated at the edges of retreating ice caps, contributions of multiple smaller congregating dust storms, and subsequent circulation of cap edge dynamics. Type C storms

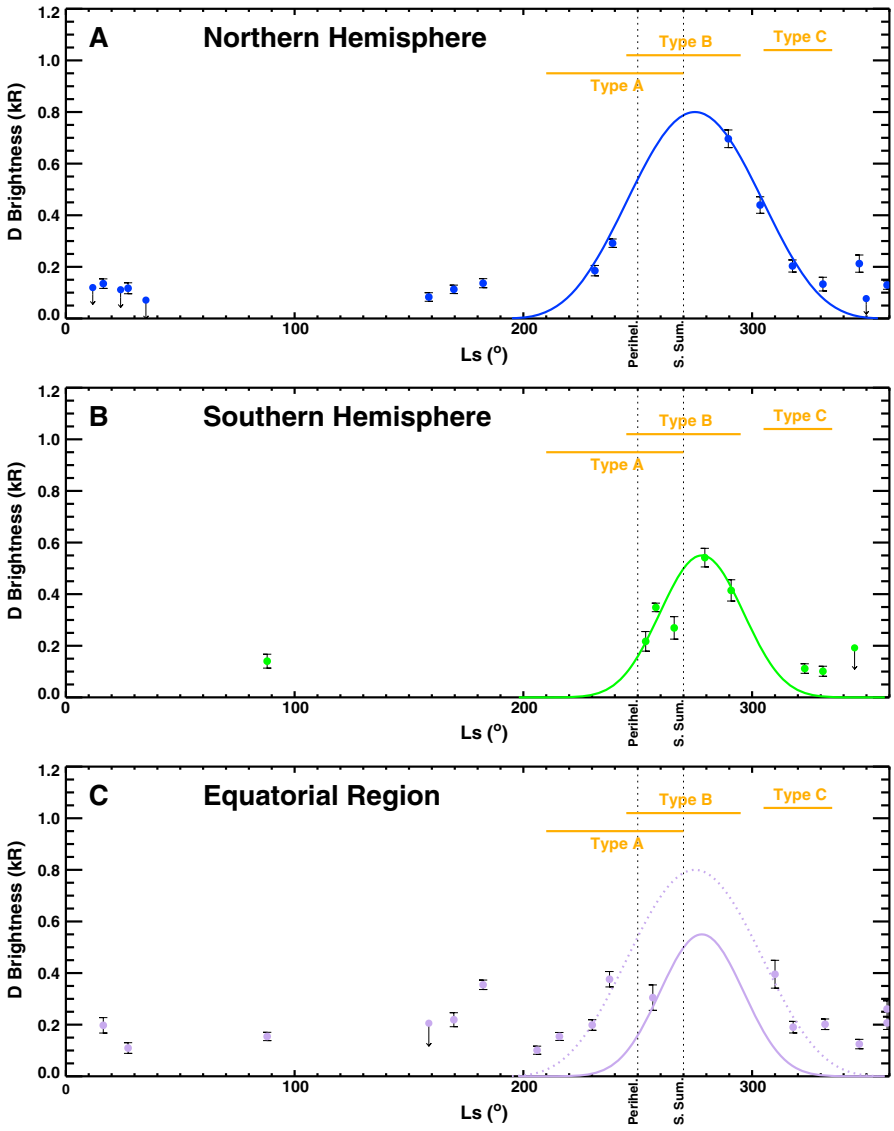

Figure 4. The brightness of deuterium Lyman α observed at the limb, over 15 Mars months, at different latitude regions. The observations are averaged to remove the effects of solar rotation and corrected for solar activity variations. The line of sight tangent point latitude was used to separate observations made over the (a) northern hemisphere (blue circles), (b) southern hemisphere (green circles), and (c) equatorial region (purple circles) of Mars. Uncertainties are shown as vertical bars. Brightness values within 3 sigma of the noise level are considered upper limits, and their uncertainties are denoted by downward pointing arrows. The times of perihelion and southern summer solstice are shown as dotted vertical lines at 250° and 270° L_s, respectively. Solid curves in Figures 4a (blue) and 4b (green) are arbitrary best fits to the observations in each latitude region. Fits from Figures 4a and 4b are shown in Figures 4c in purple dotted and solid lines, respectively, for comparison. No independent fits to the equatorial region brightness trends have been made. Markers for regional storms of three types are shown for reference (horizontal orange lines) and are discussed further in the text.

are relatively short duration, sporadic, and have the weakest heating response of the three types. The heating effects of C storms are expected to occur in both hemispheres. The typical durations for these dust storms are shown in Figure 4 for reference and are derived using the statistical averages determined in Table 1 of Kass et al. (2014).

The resulting D brightness data points derived for the northern and summer hemispheres, shown in Figure 4, show trends similar to those in Figure 3, where the D brightness is enhanced between 220° and 320° L_s. A curve is fit to the observations for each of the northern and southern hemisphere data sets. No clear trend appears in the equatorial region data set and so the fits derived for the northern and southern hemisphere

observations are shown for the equatorial region as a reference. A timescale for the variability of deuterium brightness in each hemisphere is derived using the properties of the best fit curve. The timescale used here is defined as the time, measured using L_s (where 1°–2 sol), it takes for the brightness to transition from its peak value to e^{-1} of the peak brightness.

The northern hemisphere brightness best fit curve peaks at 0.8 kR near L_s 275° and has a timescale of ~37° (74 Martian solar days (sols)). The southern hemisphere brightness best fit curve peaks at 0.55 kR near 280° L_s and has a timescale of ~25° (50 sols). The equatorial region shows more variability that is not well constrained to dust storm activity and likely includes contributions from atmospheric dynamics in adjacent latitude regions. The lack of continuity of equatorial region data points with L_s makes it difficult to discern trends at this time.

MAVEN accelerometer measurements showed enhanced thermospheric temperatures consistent with the timing of Types A and B regional dust storms in each of the 2 Mars years of observations included here (e.g., Zurek et al., 2017). In MY32, a Type A storm was observed between L_s ~218° and 250°, followed by a Type B storm observed between L_s ~250° and 280°. These storms increased the ambient temperature by ~22 K. In MY33, a Type A storm was observed between L_s ~ 218° and 240°, followed by a Type B storm between L_s ~240° and 290°. These storms increased the ambient temperature by ~30 K. No effects due to Type C storms were observed.

The times of occurrence of the regional storms detected by MAVEN accelerometer observations are consistent with previous seasonal times reported from MRO and MGS observations. MAVEN echelle observations do not yet comprehensively cover all latitude regions at the times that the three types of storms occur. However, the data points currently available show emerging trends that support consideration of storm dynamics as one possible trigger for D brightness variability.

4. Discussion

The seasonal variation of Lyman α brightness for both D and H, corrected for solar cycle variation, shows a broad enhancement centered at 286° L_s. The observed brightness peak occurred after perihelion (250° L_s.) and just past southern summer solstice (270° L_s), whereas the Lyman α solar flux simultaneously measured at Mars by EUVM peaked at perihelion in both Mars years. For the limb observations made at southern latitudes, the daily averaged solar insolation peaked around 270° L_s. For the limb observations made at northern latitudes, the daily averaged solar insolation (seasonal heating at the surface) was highly anticorrelated with the D brightness. This suggests that there may be additional drivers other than incident solar flux and orbital position of Mars that are introducing variable amounts of deuterium into the atmosphere and that may be seasonally offset from perihelion and southern summer solstice.

Seasonal variations in the neutral atmosphere of Mars, resulting from dust storms, for example, are drivers of upper atmospheric and ionospheric variability (e.g., Keating et al., 1998; Tolson et al., 2007; Zou et al., 2005). Martian dust cycles exhibit a seasonal periodicity and can affect one or both hemispheres with a timescale of several months and are likely to transport water, ice particles, and dust into the lower atmosphere (Kass et al., 2014; Zurek & Martin, 1993). Type A dust storms are initiated in the northern hemisphere and flow across the equator to southern latitudes during southern spring. The observed D brightness enhancement between 210° and 270° L_s at all latitudes (Figure 4) is consistent with this type of trigger. Type A storms have longer lasting effects in the northern hemisphere than do Type B storms in the southern hemisphere. This is consistent with the larger timescale derived for the northern hemisphere than southern hemisphere D brightness trends.

A study of water vapor variability due to dust storms concluded that observed H_2O densities and volume mixing ratios were enhanced during dust storms up to a few tens of kilometers above nominal (dust-free) conditions (Fedorova et al., 2017). Water vapor that is available at higher altitudes due to storm turbulence will subsequently photodissociate to produce hydrogen and deuterium at higher altitudes than storm-free conditions. As a result, the reservoir of volatile species becomes enhanced at higher altitudes and could lead to enhanced escape of these species (e.g., Chaffin et al., 2017).

Atmospheric heating, circulation, and eddy mixing that accompany dust storms can provide the transport of water molecules into higher altitudes where the concentration of their photodissociated byproducts, such as deuterium, becomes enhanced (Wang et al., 2005). During regional dust storms, local transport causes upwelling of lower atmospheric water vapor to higher altitudes in the southern hemisphere and meridional circulation causes adiabatic heating during downwelling of this vapor into the northern hemisphere and can lead to up to 30 K increase in thermospheric temperatures (Bougher et al., 2000; Fedorova et al., 2017). For the dust storms that occurred during the observations used here, the thermospheric temperature increased by ~22 K during MY32 and by ~30 K during MY33. If the abundance of D below 400 km is sensitive to dust storm-related temperature gradients, this could explain the larger peak brightness seen in MY33 than in MY32 (Figure 1), despite the higher solar flux incident upon the upper atmosphere of Mars in MY32.

Observations of annual water vapor column abundances at Mars show seasonal patterns with hemispherical differences (Fedorova et al., 2006; Maltagliati et al., 2013, 2011). In the southern hemisphere, water abundances peak between 250° and 300° L_s (Trokhimovskiy et al., 2015). This is attributed to transport from the northern summertime reservoirs during their peak abundance as well as to the sublimation of the southern polar cap. At equatorial regions, the water vapor abundance increases from 200° to 240° L_s and decreases between 310° and 360° L_s. The equatorial region trends in water vapor column are attributed to transport of water, dust, and ice aerosols by planetary waves as well as to transport of water from the southern hemisphere (Clancy et al., 1996; Fedorova et al., 2004; Montmessin et al., 2004).

Measurements of absolute abundances of water vapor column with season made over the past 5 Mars years have shown these trends to be repeatable (Trokhimovskiy et al., 2015). There are gaps in northern hemisphere observations of water vapor column during perihelion (when IUVS echelle data are available) and insufficient northern hemisphere observations from IUVS echelle at nonperiapse times (when water vapor column abundance observations are available) to make comparisons at this time. However, for the southern hemisphere and equatorial regions during seasonal times where overlapping observations exist, the trends in D brightness and water vapor column are similar, indicating the sensitivity of the upper atmospheric reservoir of volatiles to lower atmospheric dynamics.

5. Summary and Conclusion

The deuterium Lyman α brightness observed at the limb of Mars, up to 400 km, has been measured and examined over 15 Martian months. The resulting analysis shows that the D brightness varied sporadically with hourly to daily timescales consistent with transient events such as high solar energetic particle influx and strong flares. A 28 day variability in brightness is attributed to solar rotation and changing solar Lyman α flux. Little variation was observed due to solar cycle activity, consistent with the solar quiet conditions of the observations. When the effects of these solar-induced sources are removed by averaging over a 28 day solar rotation cycle, seasonal trends in deuterium brightness become more apparent.

Observations of D brightness, separated into three latitudinal bands, showed hemispherical differences in the timescales and duration of the D brightness enhancement that cannot be consistently explained by seasonal trends in solar Lyman α flux alone. Additional drivers of the observed D brightness variability in the upper atmosphere may be due to orbital and seasonal variations that produce regional storms, large-scale heating, circulation patterns, and lower atmospheric dynamical processes. These seasonal dynamics enhance the production of water in Mars's lower and middle atmosphere and thereby enhance the availability of deuterium from photodissociated water vapor.

Ongoing and future MAVEN observations would allow for more seasonal coverage of D and H data collection across the planet, specifically between 0° and 160° L_s. Filling in these observational data gaps would provide a broader picture of the annual variability of D (and H) brightness and allow for more comprehensive assessment (in altitude and season) of sources that are affecting atmospheric escape of water-based species.

Efforts are currently underway to numerically model the physical properties of D using the observations described here. The results of the simulations will provide number densities and/or temperatures that will supplement observations made by other instruments (e.g., the MAVEN Neutral Gas and Ion Mass Spectrometer). These properties will contribute to quantifying the D/H ratio and the processes that determine it and provide more accurate estimates of a key quantity in determining the evolution of water at Mars.

Table A1
Observational Details of Data Used in This Work

Epoch name	Orbital range	Binning scheme[a] $X \times Y$	Limb scans	Frames	Integration time (s)	Observation dates
C1A	0240–0446	201 × 18	1	60	1.4	11 December 2014 to 22 December 2014
C1B	0458–1808	160 × 50	1	30	3.4	24 December 2014 to 3 September 2015
P1A	2288–2292	160 × 50	3	14	29.4	3 December 2015 to 4 December 2015
P1B	2989–3261	512 × 92	3	14	29.4	12 April 2016 to 2 June 2016
C2A	3480–3546	384 × 64	4–8	8	29.4	13 July 2016 to 25 July 2016
C2B	3562–3850	332 × 74	4	10	29.4	28 July 2016 to 20 September 2016
P2A	3966–4167	512 × 92	3	14	29.4	12 October 2016 to 20 November 2016
P2B	4182–4186	512 × 92	5	8	29.4	23 November 2016 to 24 November 2016
P2C	4218–4222	512 × 92	4	8	29.4	30 November 2016 to 1 December 2016
C3A	4289–4542	332 × 74	1	10	29.4	13 December 2016 to 31 January 2017
C3B	4546–4804	332 × 74	4–8	8	29.4	1 February 2017 to 22 March 2017
A1A	4672–4770	332 × 74	1	168[b]	29.4	25 February 2017 to 26 March 2017
P3A	4849–5037		Same as P2A			30 March 2017 to 5 May 2017

[a]Variations in the altitudes ranges along the line of sight sampled by the different binning schemes are accounted for in the data reduction. [b]The apoapse scan includes observations of the corona, limb, and disk of the planet, similar to C-type epochs, but at a different spacecraft orbital location. Only the limb-pointed subset of apoapsis frames with MRH altitudes between 0 and 400 km was used in this work.

Appendix A

A1. Observational Details

The IUVS echelle images used in this work are publically available on the PDS. An echelle file includes images of an orbital segment referred to as a scan. Each scan includes a succession of images called "frames" taken with similar integration times. Each set of observations that had consistent binning, number of limb scans per orbit, number of frames per scan, and integration time per frame was grouped into an observational "epoch." These epochs are listed in Table A1.

Table A2
Properties of Transient Event Orbits Overlapping IUVS Echelle Observations

Event orbit number	Date (mm/dd/yyyy)	L_s (°)
Solar wind SEP		
1560	7/19/2015	16
3838	9/18/2016	240
CME SEP		
1478	7/3/2015	7
Flare		
260	11/16/2014	247
420	12/17/2014	264
506	1/2/2015	272
510	1/3/2015	273
706	2/9/2015	292
3534	7/23/2016	210
Aurora		
1600	7/26/2015	19
1640	8/2/2015	23
1648	8/4/2015	24
1682	8/10/2015	27
1686	8/10/2015	27
3520	7/20/2016	208
3524	7/21/2016	209
3832	9/16/2016	238
3602	8/4/2016	216
3614	8/6/2016	217
3764	9/3/2016	232

The first letter of the "Epoch Name" denotes the type of spacecraft-observing mode. C refers to observations made when the instrument LOS was continuously scanning the disk, limb, and corona of the planet during the spacecraft inbound and outbound orbital segments. P refers to observations made of the limb while the spacecraft was at/near periapsis. A refers to observations made of the limb while the spacecraft was at/near apoapsis. The "Orbital Range" is the span of MAVEN orbits that fall within each epoch. The "Binning Scheme" includes the number of binned spectral pixels (X) and spatial pixels (Y) used at each epoch. The "Limb Scans" column specifies the number of scans iteratively taken of the limb during one orbit of that epoch. The number of limb scans is counted for either inbound or outbound segment of an orbit, where the transition from outbound to inbound occurs at spacecraft apoapsis. The "Frames" column describes the number of continuous images captured by the echelle detector in each scan. Each image is formed by exposing the detector for a specified "Integration Time," listed in seconds. The observation dates for the data set used here are provided for reference.

IUVS echelle data files with Epoch files denoted with a "C" are labeled as *outbound*, *inlimb*, or *outlimb* in the PDS filenames. Epoch files denoted with a "P" are labeled as *periapse*. Epoch files denoted with an "A" are labeled as *apoapse*. Due to early mission file naming conventions, some outbound labeled echelle files include observations of the disk and corona as well as the limb of Mars. The limb data files of these early orbits are the second outbound labeled data file in the time series of outbound files for that orbit.

A2. Transient Event Details

MAVEN recorded multiple solar flare and energetic particle events throughout its orbit about Mars. Lists of solar-originating disturbances measured by MAVEN are provided in Thiemann et al. (2015), Lee et al. (2017), and in https://lasp.colorado.edu/maven/sdc/public/pages/notebook/events/index.html. The dates and L_s corresponding to the orbits of the transient events that overlapped with D echelle measurements discussed in this work are listed in Table A2.

Acknowledgments
The authors would like to thank the reviewers for their constructive comments and suggestions. M. M. and J. C. thank S. Bougher and A. Fedorova for valuable discussions. This work was funded by NASA Contract 1000320450 from the University of Colorado to Boston University. The MAVEN IUVS data used here are available on the NASA Planetary Data System at http://atmos.nmsu.edu/data_and_services/atmospheres_data/MAVEN/calib.html. Information pertinent to reproduction of the results shown here are provided in Appendix A.

References

Ajello, J., Pryor, W., Barth, C., Hord, C., Stewart, A., Simmons, K., & Hall, D. (1994). Observations of interplanetary Lyman-α with the Galileo ultraviolet spectrometer: Multiple scattering effects at solar maximum. *Astronomy and Astrophysics*, *289*, 283–303.

Aleshin, V. I. (2004). Numerical simulation of seasonal dynamics of water vapor in the Martian atmosphere. *Solar System Research*, *38*(6), 434–440. https://doi.org/10.1007/s11208-005-0011-8

Aoki, S., Nakagawa, H., Sagawa, H., Giuranna, M., Sindoni, G., Aronica, A., & Kasaba, Y. (2015). Seasonal variation of the HDO/H_2O ratio in the atmosphere of Mars at the middle of northern spring and beginning of northern summer. *Icarus*, *260*, 7–22. https://doi.org/10.1016/j.icarus.2015.06.021

Benna, M., Mahaffy, P. R., Grebowsky, J. M., Plane, J. M. C., Yelle, R. V., & Jakosky, B. M. (2015). Metallic ions in the upper atmosphere of Mars from the passage of comet C/2013 A1 (siding spring). *Geophysical Research Letters*, *42*(12), 4670–4675. https://doi.org/10.1002/2015GL064159

Bertaux, J.-L., Clarke, J., Mumma, M., Owen, T., & Quemerais, E. (1992). A search for the deuterium Lyman-alpha emission from the atmosphere of Mars. In P. Benvenuti & E. J. Schreier (Eds.), *ESO Conference and Workshop Proceedings*, 44 (459 pp.).

Bertaux, J.-L., Leblanc, F., Witasse, O., Quemerais, E., Lilensten, J., Stern, A., … Korablev, O. (2005). Discovery of an aurora on Mars. *Nature*, *435*(7043), 790–794. https://doi.org/10.1038/nature03603

Bertaux, J. L., & Montmessin, F. (2001). Isotopic fractionation through water vapor condensation: The deuterophase, a cold trap for deuterium in the atmosphere of Mars. *Journal of Geophysical Research*, *106*(E12), 32,879–32,884. https://doi.org/10.1029/2000JE001358

Bhattacharyya, D., Clarke, J. T., Bertaux, J.-L., Chaufray, J.-Y., & Mayyasi, M. (2015). A strong seasonal dependence in the Martian hydrogen exosphere. *Geophysical Research Letters*, *42*(20), 8678–8685. https://doi.org/10.1002/2015GL065804

Bhattacharyya, D., Clarke, J., Bertaux, J.-L., Chaufray, J.-Y., & Mayyasi, M. (2017). Analysis and modeling of remote observations of the Martian hydrogen exosphere. *Icarus*, *281*, 264–280. https://doi.org/10.1016/j.icarus.2016.08.034

Bougher, S., Engel, E., Roble, R., & Foster, B. (2000). Comparative terrestrial planet thermospheres. 3. Solar cycle variation of global structure and winds at solstices. *Journal of Geophysical Research*, *105*(E7), 17,669–17,692. https://doi.org/10.1029/1999JE001232

Bruner, E., & Wilson, T. (1969). Deuterium in the Earth's exosphere. *Journal of Geophysical Research*, *74*(26), 6491–6493. https://doi.org/10.1029/JA074i026p06491

Chaffin, M., Chaufray, J.-Y., Stewart, I., Montmessin, F., Schneider, N., & Bertaux, J.-L. (2014). Unexpected variability of Martian hydrogen escape. *Geophysical Research Letters*, *41*(2), 314–320. https://doi.org/10.1002/2013GL058578

Chaffin, M., Deighan, J., Schneider, N., & Stewart, I. (2017). Elevated atmospheric water escape of atomic hydrogen from Mars induced by high-altitude water. *Nature Geoscience*, *10*(3), 174–178. https://doi.org/10.1038/ngeo2887

Chaufray, J.-Y., Gonzalez-Galindo, F., Forget, F., Lopez-Valverde, M., Leblanc, F., Modolo, R., & Hess, S. (2015). Variability of the hydrogen in the Martian upper atmosphere as simulated by a 3D atmosphere-exosphere coupling. *Icarus*, *245*, 282–294. https://doi.org/10.1016/j.icarus.2014.08.038

Clancy, R., Grossman, A., Wolff, M., James, P., Rudy, D., Billawala, Y., … Muhleman, D. (1996). Water vapor saturation at low altitudes around Mars aphelion: A key to Mars climate? *Icarus*, *122*(1), 36–62. https://doi.org/10.1006/icar.1996.0108

Clarke, J. T., Bertaux, J.-L., Chaufray, J.-Y., Gladstone, G. R., Quemerais, E., Wilson, J. K., & Bhattacharyya, D. (2014). A rapid decrease of the hydrogen corona of Mars. *Geophysical Research Letters*, *41*(22), 8013–8020. https://doi.org/10.1002/2014GL061803

Clarke, J. T., Bertaux, J.-L., Chaufray, J.-Y., Owen, T., Nagy, A., & Gladstone, G. R. (2006). HST/STIS observations of the D/H ratio in the Martian upper atmosphere. *Bulletin of the American Astronomical Society*, *38*, 600.

Clarke, J. T., Lallement, R., Bertaux, J.-L., Fahr, H., Quémerais, E., & Scherer, H. (1998). HST/GHRS observations of the velocity structure of interplanetary hydrogen. *The Astrophysical Journal*, *499*(1), 482–488. https://doi.org/10.1086/305628

Clarke, J. T., Mayyasi, M., Bhattacharyya, D., Schneider, N. M., McClintock, W. E., Deinghan, J. L., … Jakosky, B. M. (2017). Variability of D and H in the Martian upper atmosphere observed with the MAVEN IUVS echelle channel. *Journal of Geophysical Research: Space Physics*, *122*, 2336–2344. https://doi.org/10.1002/2016JA023479

Donahue, T. (1969). Deuterium in the upper atmosphere of Venus and Earth. *Journal of Geophysical Research*, *74*(5), 1128–1137. https://doi.org/10.1029/JA074i005p01128

de Bergh, C. (1992). The D/H ratio and the evolution of water in the terrestrial planets. *Origins of Life and Evolution of the Biosphere*, *23*, 11–21.

Eparvier, F., Chamberlin, P., Woods, T., & Thiemann, E. (2015). The solar extreme ultraviolet monitor for MAVEN. *Space Science Reviews*, *195*(1-4), 293–301. https://doi.org/10.1007/s11214-015-0195-2

Fedorova, A., Bertaux, J.-L., Betsis, D., Montmessin, F., Korablev, O., Maltagliati, L., & Clarke, J. (2017). Water vapor in the middle atmosphere of Mars during the 2007 global dust storm. *Icarus*, *300*, 440–457.

Fedorova, A., Korablev, O., Bertaux, J.-L., Rodin, A., Kiselev, A., & Perrier, S. (2006). Mars water vapor abundance from SPICAM IR spectrometer: Seasonal and geographic distributions. *Journal of Geophysical Research*, *111*, E09S08. https://doi.org/10.1029/2006JE002695

Fedorova, A., Rodin, A., & Baklanova, I. (2004). MAWD observations revisited: Seasonal behavior of water vapor in the Martian atmosphere. *Icarus*, *171*(1), 54–67. https://doi.org/10.1016/j.icarus.2004.04.017

Fernández, W. (1998). Martian dust storms: A review. *Earth, Moon, and Planets*, *77*, 19–46.

Fröhlich, C., & Lean, J. (2004). Solar radiative output and its variability: Evidence and mechanisms. *Astronomy and Astrophysics Review*, *12*(4), 273–320. https://doi.org/10.1007/s00159-004-0024-1

Haberle, R. M., & Jakosky, B. M. (1990). Sublimation and transport of water from the north residual polar cap on Mars. *Journal of Geophysical Research*, *95*(B2), 1423–1437. https://doi.org/10.1029/JB095iB02p01423

Haider, S., Mahajan, K., & Kallio, E. (2011). Mars ionosphere: A review of experimental results and modeling results. *Reviews of Geophysics*, *49*, RG4001. https://doi.org/10.1029/2011RG000357

Halekas, J. S. (2017). Seasonal variability of the hydrogen exosphere of Mars. *Journal of Geophysical Research: Planets*, *122*(5), 901–911. https://doi.org/10.1002/2017JE005306

Halekas, J. S., Taylor, E. R., Dalton, G., Johnson, G., Curtis, D. W., McFadden, J. P., … Jakosky, B. M. (2015). The solar wind ion analyzer for MAVEN. *Space Science Reviews*, *195*(1-4), 125–151. https://doi.org/10.1007/s11214-013-0029-z

Head, J., & Marchant, D. (2014). The climate history of early Mars: Insights from the Antarctic McMurdo Dry Valleys hydrologic system. *Antarctic Science*, *26*(06), 774–800. https://doi.org/10.1017/S0954102014000686

Jakosky, B. M. (1983). The role of seasonal reservoirs in the Mars water cycle: II. Coupled models of the regolith, the polar caps, and atmospheric transport. *Icarus*, *55*(1), 19–39. https://doi.org/10.1016/0019-1035(83)90047-7

Jakosky, B. M. (1991). Mars volatile evolution: Evidence from stable isotopes. *Icarus*, *94*(1), 14–31. https://doi.org/10.1016/0019-1035(91)90138-J

Jakosky, B. (2015). MAVEN explores the Martian upper atmosphere. *Science*, *350*(6261), 643. https://doi.org/10.1126/science.aad3443

Jakosky, B. M., & Farmer, C. B. (1982). The seasonal and global behavior of water vapor in the Mars atmosphere: Complete global results of the *Viking* atmospheric water detector experiment. *Journal of Geophysical Research*, *87*(B4), 2999–3019. https://doi.org/10.1029/JB087iB04p02999

Kass, D., Kleinböhl, A., McCleese, D., Schofeild, J., & Smith, M. (2014). Interannual Behavior of Large Regional Dust Storms. In *Eight International Conference on Mars* (LPI Contribution No. 1791, 1169 pp.). Pasadena, CA. 14–18 July.

Keating, G., Bougher, S. W., Zurek, R. W., Tolson, R. H., Cancro, G. J., Noll, S. N., … Babicke, J. M. (1998). The structure of the upper atmosphere of Mars: In situ accelerometer measurements from Mars Global Surveyor. *Science*, *279*(5357), 1672–1676. https://doi.org/10.1126/science.279.5357.1672

Krasnopolsky, V. A. (2015). Variations of the HDO/H_2O ratio in the Martian atmosphere and loss of water from Mars. *Icarus*, *257*, 377–386. https://doi.org/10.1016/j.icarus.2015.05.021

Krasnopolsky, V. A., Mumma, M. J., & Gladstone, G. R. (1998). Detection of atomic deuterium in the upper atmosphere of Mars. *Science*, *280*(5369), 1576–1580. https://doi.org/10.1126/science.280.5369.1576

Larson, D., Lillis, R., Lee, C., Dunn, P., Hatch, K., Robinson, M., … Jakosky, B. (2015). The MAVEN solar energetic particle investigation. *Space Science Reviews*, *195*(1-4), 153–172. https://doi.org/10.1007/s11214-015-0218-z

Lee, C. O., Hara, T., Halekas, J. S., Thiemann, E., Chamberlin, P., Eparvier, F., … Jakosky, B. M. (2017). MAVEN observations of the solar cycle 24 space weather conditions at Mars. *Journal of Geophysical Research: Space Physics*, *122*, 2768–2794. https://doi.org/10.1002/2016JA023495

Mahaffy, P., Webster, C. R., Stern, J. C., Brunner, A. E., Atreya, S. K., Conrad, P. G., … the MSL Science Team (2015). The imprint of atmospheric evolution in the D/H of Hesperian clay minerals on Mars. *Science*, *347*(6220), 412–414. https://doi.org/10.1126/science.1260291

Maltagliati, L., Montmessin, F., Korablev, O., Fedorova, A., Forget, F., Määttänen, A., … Bertaux, J.-L. (2013). Annual survey of water vapor vertical distribution and water–aerosol coupling in the Martian atmosphere observed by SPICAM/MEx solar occultations. *Icarus*, *223*(2), 942–962. https://doi.org/10.1016/j.icarus.2012.12.012

Maltagliati, L., Titov, D., Encrenaz, T., Melchiorri, R., Forget, F., Keller, H., & Bibring, J.-P. (2011). Annual survey of water vapor behavior from the OMEGA mapping spectrometer onboard Mars Express. *Icarus*, *213*(2), 480–495. https://doi.org/10.1016/j.icarus.2011.03.030

Mayyasi, M., Clarke, J., Quénerais, E., Katushkina, O., Bhattacharyya, D., Chaufray, J.-Y., … Jakosky, B. (2017). IUVS echelle-mode observations of interplanetary hydrogen: Standard for calibration and reference for cavity variations between Earth and Mars during MAVEN cruise. *Journal of Geophysical Research: Space Physics*, *122*, 2089–2105. https://doi.org/10.1002/%202016JA023466

McClintock, W., Schneider, N. M., Holsclaw, G. M., Clarke, J. T., Hoskins, A. C., Stewart, I., … Deighan, J. (2015). The Imaging Ultraviolet Spectrograph (IUVS) for the MAVEN mission. *Space Science Reviews*, *195*(1-4), 75–124. https://doi.org/10.1007/s11214-014-0098-7

McElroy, M. B., & Donahue, T. M. (1972). Stability of the Martian atmosphere. *Science*, *177*(4053), 986–988. https://doi.org/10.1126/science.177.4053.986

Montmessin, F., Forget, F., Rannou, P., Cabane, M., & Haberle, R. (2004). Origin and role of water ice clouds in the Martian water cycle as inferred from a general circulation model. *Journal of Geophysical Research*, *105*(E2), E10004. https://doi.org/10.1029/2004JE002284

Montmessin, F., Fouchet, T., & Forget, F. (2005). Modeling the annual cycle of HDO in the Martian atmosphere. *Journal of Geophysical Research*, *110*, E03006(E3). https://doi.org/10.1029/2004JE002357

Novak, R., Mumma, M., & Villanueva, G. (2011). Measurement of the isotopic signatures of water on Mars: Implications for studying methane. *Planetary and Space Science*, *59*(2-3), 163–168. https://doi.org/10.1016/j.pss.2010.06.017

Owen, T., Maillard, J. P., de Bergh, C., & Lutz, B. (1988). Deuterium on Mars: The abundance of HDO and the value of D/H. *Science*, *240*(4860), 1767–1770. https://doi.org/10.1126/science.240.4860.1767

Quémerais, E., Izmodenov, V. V., Koutroumpa, D., & Malama, Y. (2008). Time dependent model of the interplanetary Lyman α glow: Applications to the SWAN data. *Astronomy and Astrophysics*, *488*(1), 351–359. https://doi.org/10.1051/0004-6361:20078204

Schneider, N., Jain, S., Deighan, J., Stewart, I., Stiepen, A., Larson, D., … Jakosky, B. (2017). Three types of aurora on Mars, *International Conference on Mars Aeronomy*, Boulder, CO, May 2017.

Tamppari, L., Zurek, R., & Paige, D. (2003). Viking-era diurnal water-ice clouds. *Journal of Geophysical Research*, *108*(E7), 5073. https://doi.org/10.1029/2002JE001911

Thiemann, E. M. B., Eparvier, F. G., Andersson, L. A., Fowler, C. M., Peterson, W. K., Mahaffy, P. R., … Jakosky, B. M. (2015). Neutral density response to solar flares at Mars. *Geophysical Research Letters*, *42*(21), 8986–8992. https://doi.org/10.1002/2015GL066334

Thiemann, E. M. B., Chamberlin, P. C., Eparvier, F. G., Templeman, B., Woods, T. N., Bougher, S. W., & Jakosky, B. M. (2017). The MAVEN EUVM model of solar spectral irradiance variability at Mars: Algorithms and results. *Journal of Geophysical Research: Space Physics*, *122*, 2748–2767. https://doi.org/10.1002/2016JA023512

Tolson, R., Keating, G., Zurek, R., Bougher, S., Justus, C., & Fritts, D. (2007). Application of accelerometer data to atmospheric modeling during Mars aerobreaking operations. *Journal of Spacecraft and Rockets*, *44*(6), 1172–1179. https://doi.org/10.2514/1.28472

Trokhimovskiy, A., Fedorova, A., Korablev, O., Montmessin, F., Bertaux, J.-L., Rodin, A., & Smith, M. (2015). Mars' water vapor mapping by the SPICAM IR spectrometer: Five Martian years of observations. *Icarus*, *251*, 50–64. https://doi.org/10.1016/j.icarus.2014.10.007

Villanueva, G., Mumma, M., Bonev, B., Novak, R., Barber, R., & DiSanti, M. (2012). Water in planetary and cometary atmospheres: H_2O/HDO transmittance and fluorescence models. *Journal of Quantitative Spectroscopy and Radiation Transfer*, *113*(3), 202–220. https://doi.org/10.1016/j.jqsrt.2011.11.001

Villanueva, G., Mumma, M., Novak, R., Käufl, H., Hartogh, P., Encrenaz, T., … Smith, M. (2015). Strong water isotopic anomalies in the Martian atmosphere: Probing current and ancient reservoirs. *Science*, *348*(6231), 218–221. https://doi.org/10.1126/science.aaa3630

Wang, H., Zurek, R., & Richardson, M. (2005). Relationship between frontal dust storms and transient eddy activity in the Northern Hemisphere of Mars as observed by Mars Global Surveyor. *Journal of Geophysical Research*, *110*, E07005. https://doi.org/10.1029/2005JE002423

Webster, C., Mahaffy, P. R., Flesch, G. J., Niles, P. B., Jones, J. H., Leshin, L. A., … the MSL Science Team (2013). Isotope ratios of H, C, and O in CO_2 and H_2O of the Martian atmosphere. *Science*, *341*(6143), 260–263. https://doi.org/10.1126/science.1237961

Withers, P., & Pratt, R. (2013). An observational study of the response of the upper atmosphere of Mars to lower atmospheric dust storms. *Icarus*, *225*(1), 378–389. https://doi.org/10.1016/j.icarus.2013.02.032

Yung, Y., Wen, J.-S., Pinto, J., Allen, M., Pierce, K., & Paulson, S. (1988). HDO in the Martian atmosphere: Implications for the abundance of crustal water. *Icarus*, *76*(1), 146–159. https://doi.org/10.1016/0019-1035(88)90147-9

Zou, H., Wang, J.-S., & Nielsen, E. (2005). Effect of the seasonal variations in the lower atmosphere on the altitude of the ionospheric main peak at Mars. *Journal of Geophysical Research*, *110*, A09311. https://doi.org/10.1029/2004JA010963

Zurek, R., & Martin, L. (1993). Interannual variability of planet-encircling dust storms on Mars. *Journal of Geophysical Research*, *98*(E2), 3247–3259. https://doi.org/10.1029/92JE02936

Zurek, R. W., Tolson, R. A., Bougher, S. W., Lugo, R. A., Baird, D. T., Bell, J. M., & Jakosky, B. M. (2017). Mars thermosphere as seen in MAVEN accelerometer data. *Journal of Geophysical Research: Space Physics*, *122*, 3798–3814. https://doi.org/10.1002/2016JA023641